

A current control method for bidirectional multiphase DC-DC boost-buck converter

Gifari Iswandi Hasyim, Sulisty Wijanarko, Jihad Furqani, Arwindra Rizqiawan, Pekik Argo Dahono

School of Electrical Engineering and Informatics, Institut Teknologi Bandung, Bandung, Indonesia

Article Info

Article history:

Received Nov 4, 2021

Revised Dec 15, 2021

Accepted Jan 2, 2022

Keywords:

Battery
Control
DC-DC converter
Energy storage
Renewable energy

ABSTRACT

In the future, more and more electric vehicle (EV) batteries are connected to the direct current (DC) microgrid. Depending on the battery state of charge, the battery voltage can be higher or lower than the DC microgrid voltage. A converter that is aimed to fulfil such function must be capable of working in both charging and discharging regardless the voltage level of the battery and DC microgrid. Battery performance degradation due to ripple current entering the battery is also a concern. In this paper, a converter that can minimize ripple current that entering battery and operate in two power-flow directions regardless of battery and DC microgrid voltage level is presented. A current control method for this kind of converter was proposed. Experiment on a prototype was conducted to prove the proposed converter current control method.

This is an open access article under the [CC BY-SA](https://creativecommons.org/licenses/by-sa/4.0/) license.



Corresponding Author:

Gifari Iswandi Hasyim

School of Electrical Engineering and Informatics, Institut Teknologi Bandung

Jalan Ganesa No. 10, Lebak Siliwangi, Coblong, Bandung, Jawa Barat 40132, Indonesia

Email: gifarihasyim@gmail.com

1. INTRODUCTION

Utilization of renewable energy to fill energy demand give rise to many distributed generators. According to conventional way of electric power transmission and distribution, these distributed generators must be connected first to the main grid before their produced outputs are able to be transmitted and distributed to various users. The problem with this approach is a large investment is required to connect these distributed generators to the main grid. One way to take advantage of these distributed generators, without having to integrate them to the main grid, is to build a microgrids near these distributed generators and connect them to this microgrid. Loads around the microgrid can be supplied by distributed generators without having to rely on the main grid to distribute the generated electricity. Since most of the electricity generated by renewable energy sources is in the form of direct current, direct current (DC) microgrids are a suitable choice for delivering electricity from these distributed generators to the local loads. Compared to an alternating current (AC) grid, a DC grid has several advantages such as the absence of problems with reactive power and synchronization [1]–[3].

Figure 1 shows a DC microgrid system. Various renewable energy sources, energy storage system, and loads is connected to the DC microgrid. The energy storage systems will absorb excess electricity generated by renewable energy sources and will release it back to the DC microgrid when needed. Energy storage systems can be in the form of batteries or electric vehicle (EV) batteries [4], [5].

One issue of EV batteries is their lifetime [6], [7]. Ripple current is one factor that fade battery capacity and increase its impedance. Variation of capacity and impedance of each cell can cause voltage difference between cells. Voltage difference between cells can cause heat problem because of possibility differential current flows from one cell to other cell [8]. Ripple currents occur from switching of power

electronics converter connected to the battery. Hence, reducing ripple current entering a battery is urgent. One way to reduce the ripple current is to employ multiphases topology of a converter [9], [10].

Fluctuation of DC microgrid voltage and ever-changing EV battery's state of charge (SoC) make it possible for the battery voltage to be higher or lower than the DC microgrid voltage. This phenomenon, which is called as 'overlapping' in some literature [11], implies that DC-DC power converter plays an important role in ensuring energy transfer between EV batteries and DC microgrid happens [12]. Various converter topology for aiding in bidirectional energy transfer between battery and DC microgrid has been reviewed in [13] but none of them concerned about overlapping phenomenon. Converter that can facilitate power exchange between EV battery and DC microgrid under possibilities of overlapping condition has been proposed in [11], [14]–[16] but this converter still doesn't address the current ripple problem. The converter proposed by [17]–[19] can work in both direction and when either the battery voltage is higher or lower than DC microgrid voltage, but have non-continuous current so the ripple current is still large.

In this paper, the proposed converter, and its control strategy for interfacing battery between DC microgrid and battery is explained. The proposed converter can direct power flows between battery and DC microgrid whether it is for charging or discharging the battery, can work regardless of the battery voltage level relative to the DC microgrid voltage and also has minimization mechanism for the ripple current that flows through battery so the battery performance will not be degraded. This paper is organized as follow: section 1 introduces about current trends in renewable energy and microgrid; section 2 describes the proposed converter; section 3 explains the modelling of the proposed converter and issue regarding the control system of the proposed converter; section 4 describes the current controller of the proposed converter; section 5 presents the experimental results from a prototype to demonstrate the proposed converter capabilities; and section 6 concludes this paper.

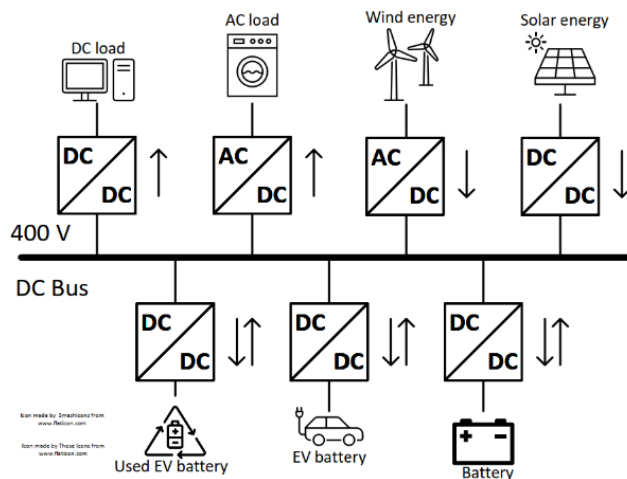


Figure 1. DC microgrid system

2. THE PROPOSED CONVERTER

The proposed converter is called multiphases DC-DC boost-buck converter. The proposed converter objective is limited to regulate the power flow between a battery and a DC microgrid and at the same time minimize ripple current entering the battery. The derivation of the proposed converter will be presented to understand how the converter came into being. Knowledge of derivation of the proposed converter also helps in understanding how this converter is capable to deliver its objective. Figure 2 shows 2 kinds of boost-buck converter. Figure 2(a) shows a single-phase DC-DC boost-buck converter. The output voltage of the converter under continuous conduction mode is:

$$v_o(t) = \frac{d(t)}{1-c(t)} v_i(t) \quad (1)$$

where $v_i(t)$, $c(t)$, $d(t)$ and $v_o(t)$ is battery voltage, A-part duty cycle, B-part duty cycle, and DC microgrid voltage, respectively. Assuming the direction of current is as shown in Figure 2(a), A-part and B-part can be regarded as a boost and a buck converter. It can be seen that the DC microgrid voltage can be higher or lower than the battery voltage. It should be noted that the switching frequencies of A-part and

B-part can be different to optimize the converter efficiency. Moreover, the duty cycles of the A-part and B-part sides can also be different.

Cascaded boost-buck converter in Figure 2(a) has solved bidirectional energy transfer problem but still does not address ripple current entering the battery. To minimize the battery and DC microgrid ripple current, the converter can be modified into the multiphase converter as shown in Figure 2(b) [9]. The phase numbers of A-part and B-part don't need to be the same. This leaves optimization room if one wish to improve the efficiency of the converter. If the duty cycle of A-part is fixed, that is $c(t)$ is kept at a constant value that results in zero ripple, then the B-part is the only one left with authority to control DC microgrid current so its duty cycle must be let to vary. On the other hand, if minimum DC microgrid ripple current is desired then B-part duty cycle is fixed (which means $d(t)$ is now kept constant instead of $c(t)$) at a certain value that results in zero ripple current. This leaves A-part to control the battery current by letting its duty cycle $c(t)$ to vary.

In this paper application, it is desirable to have minimum battery ripple current, so the duty cycle of A-part is kept constant at a certain value that results in zero ripple and its number of phases is more than one. This leaves The DC microgrid current to be controlled by B-part's duty cycle. Since the DC microgrid ripple current is not required to be low, a single-phase converter can assume a place in B-part. For this paper purpose, it is found that A-part can deliver its objective by using three phases. This leads to $1/3$ or $2/3$ to be duty cycle value that will give minimum battery ripple current. Figures 3(a) and 3(b) shows modelling of the proposed boost-buck converter. Figure 3(a) shows the proposed multiphase boost-buck converter. A-part's task is to minimize battery ripple current, so it consists of 3 phase ($m = 3$) and has constant duty cycle of $\bar{C} = 1/3$. This is shown in Figure 4 where each phase and the battery current are plotted. It can be seen that the battery current has near to zero ripple current. B-part's task is to control the DC microgrid current and it consist of one phase ($n=1$) with varying duty cycle $d(t)$. To further optimize the proposed converter in terms of weight and size, one can use the stator winding of EV traction motor as filter inductor. The EV traction motor type can be either synchronous, induction, or switch reluctance. Doing so will turn the proposed converter into 'integrated charger' [20], [21].

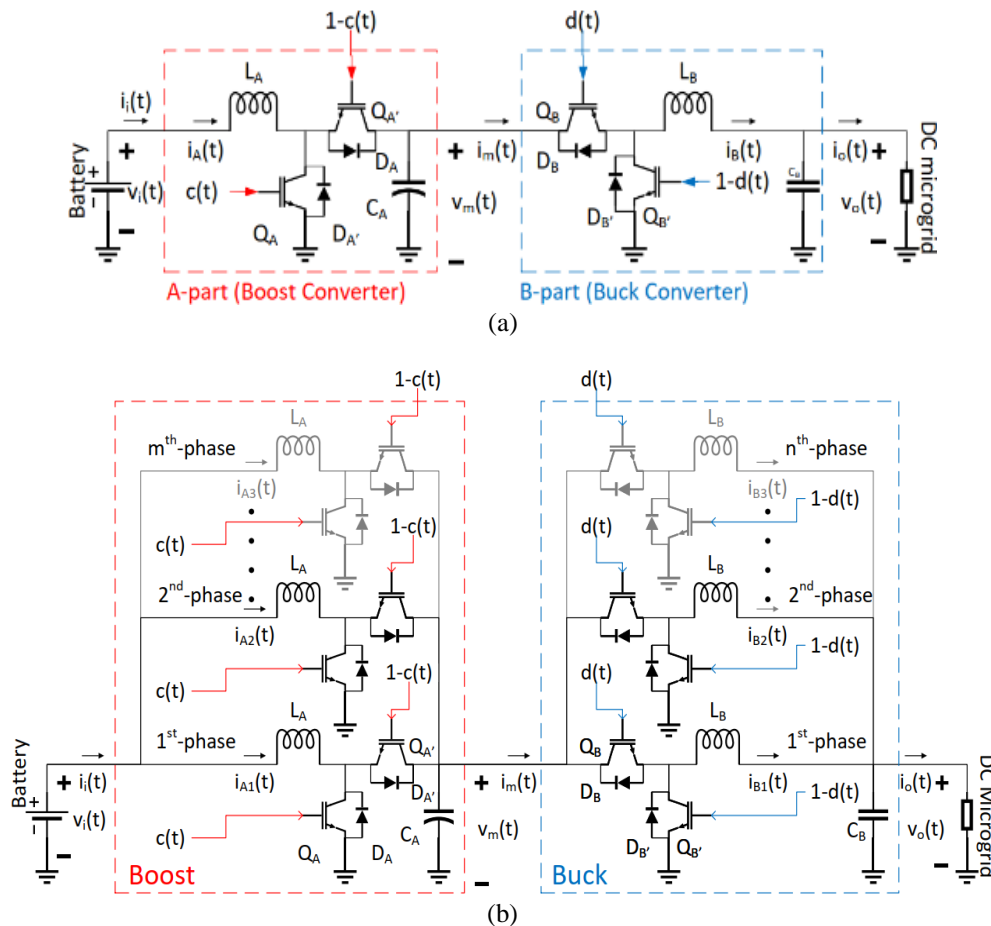


Figure 2. Boost-buck converter: (a) single phase and (b) multiphase

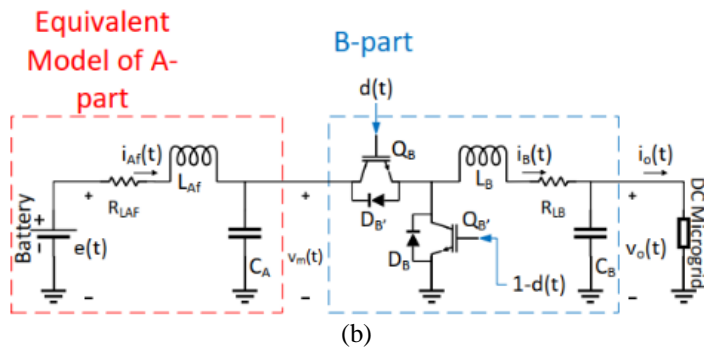
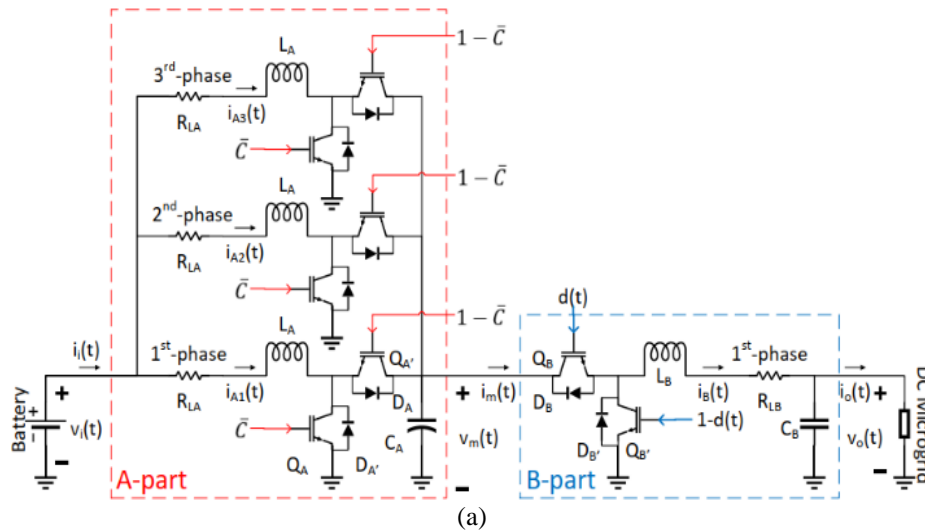


Figure 3. The proposed converter (a) real circuit and (b) equivalent model

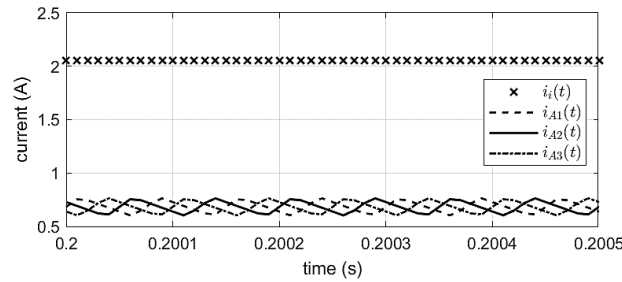


Figure 4. Battery current and A-part phase currents

3. MODELLING OF THE PROPOSED CONVERTER

Before designing the control for the proposed converter, a model of the proposed converter must be derived first. Some properties of the proposed converter can be exploited to simplify the model. A-part can be regarded as an LC filter by fact that each leg of the A-part is switched in a manner such that each leg’s duty cycle value is identical and is shifted by identical phase angle. The resulting simplification of the proposed converter is shown in Figure 3(b). The relationship between parameter in Figures 3(a) and 3(b) is given by (2) through (5):

$$e(t) = \frac{v_i(t)}{1 - \bar{c}} \tag{2}$$

$$L_{Af} = \frac{L_A}{3(1 - \bar{c})^2} \tag{3}$$

$$i_{Af}(t) = (1 - \bar{C})i_A(t) \quad (4)$$

$$R_{LAf} = \frac{R_{LA}}{3(1-\bar{C})^2} \quad (5)$$

where \bar{C} is the value of constant duty cycle and equals 1/3. The DC microgrid voltage is assumed to be a voltage source $v_o(t)$. Using state space averaging [22], The state space representation of the equivalent model of the proposed converter in Figure 3 is given by (6):

$$\begin{cases} L_B \frac{di_B(t)}{dt} = v_m(t)d(t) - v_o(t) - i_B(t)R_{LB} \\ C_A \frac{dv_m(t)}{dt} = i_{Af}(t) - i_B(t)d(t) \\ L_{Af} \frac{di_{Af}(t)}{dt} = e(t) - v_m(t) - i_{Af}(t)R_{LAf} \end{cases} \quad (6)$$

where all variables are the same as shown in Figure 3.

The current controller will be designed based on the linearization of (6). By taking the \bar{v}_m , \bar{D} , \bar{E} , \bar{V}_o , \bar{i}_{Af} and \bar{i}_B as operating point or linearization point of $v_m(t)$, $d(t)$, $e(t)$, $v_o(t)$ and $i_B(t)$, the linearized model of the proposed converter is given by (7):

$$\begin{cases} L_B \frac{d\hat{i}_B(t)}{dt} = \bar{V}_m \hat{d}(t) + \hat{v}_m(t)\bar{D} - \hat{v}_o(t) - \hat{i}_B(t)R_{LB} \\ C_A \frac{d\hat{v}_m(t)}{dt} = \hat{i}_{Af}(t) - \bar{i}_B \hat{d}(t) - \hat{i}_B(t)\bar{D} \\ L_{Af} \frac{d\hat{i}_{Af}(t)}{dt} = \hat{e}(t) - \hat{v}_m(t) - \hat{i}_{Af}(t)R_{LAf} \end{cases} \quad (7)$$

where $\hat{i}_B(t)$, $\hat{v}_m(t)$, $\hat{i}_{Af}(t)$, $\hat{d}(t)$, $\hat{v}_m(t)$, $\hat{v}_o(t)$, and $\hat{e}(t)$ are small signal of $i_B(t)$, $v_m(t)$, $i_{Af}(t)$, $d(t)$, $v_m(t)$, $v_o(t)$, and $e(t)$ respectively. Operating point of the linearized model in (7) is obtained by calculating steady state value of (6) and is given by (8):

$$\begin{cases} \bar{i}_B = (\bar{E}\bar{D} - \bar{V}_o)/(R_{LB} + \bar{D}^2 R_{LAf}) \\ \bar{v}_m = (\bar{E}R_{LB} + \bar{D}\bar{V}_o R_{LAf})/(R_{LB} + \bar{D}^2 R_{LAf}) \\ \bar{i}_{Af} = \bar{D}(\bar{E}R_{LB} + \bar{D}\bar{V}_o R_{LAf})/(R_{LB} + \bar{D}^2 R_{LAf}) \end{cases} \quad (8)$$

Also, note that from (2), another relationship can be derived and is shown in (9):

$$\bar{E} = \frac{\bar{V}_L}{1-\bar{C}} \quad (9)$$

where \bar{V}_L is operating point of the battery.

Control-to-current transfer function, $G_{id}(s)$, is obtained by taking Laplace transform of (7) and solving for $I_B(s)$ and is given by (10):

$$G_{id}(s) = \frac{I_B(s)}{D(s)} \Big|_{E(s)=0, V_o(s)=0} = \frac{\bar{v}_m - \bar{D}\bar{i}_B R_{LAf} + (\bar{v}_m C_A R_{LAf} - \bar{D}\bar{i}_B L_{Af})s + \bar{v}_m C_A L_{Af} s^2}{R_{LB} + \bar{D}^2 R_{LAf} + (L_B + \bar{D}^2 L_{Af} + C_A R_{LAf} R_{LB})s + (C_A L_{Af} R_{LB} + C_A L_B R_{LAf})s^2 + L_B C_A L_{Af} s^3} \quad (10)$$

where $I_B(s)$ and $D(s)$ are Laplace transform of $\hat{i}_B(t)$ and $\hat{d}(t)$. Battery-to-current transfer function, $G_{ie}(s)$, and DC microgrid-to-current transfer function, $G_{io}(s)$, can also be obtained by similar fashion and is given by (11) and (12):

$$G_{ie}(s) = \frac{I_B(s)}{E(s)} \Big|_{D(s)=0, V_o(s)=0} = \frac{\bar{D}}{R_{LB} + \bar{D}^2 R_{LAf} + (L_B + \bar{D}^2 L_{Af} + C_A R_{LAf} R_{LB})s + (C_A L_{Af} R_{LB} + C_A L_B R_{LAf})s^2 + L_B C_A L_{Af} s^3} \quad (11)$$

$$G_{io}(s) = \frac{I_B(s)}{V_o(s)} \Big|_{D(s)=0, E(s)=0} = \frac{-(1+C_A L_A f s^2 + C_A R_{LA} f s)}{R_{LB} + \bar{D}^2 R_{LA} f + (L_B + \bar{D}^2 L_A f + C_A R_{LA} f R_{LB})s + (C_A L_A f R_{LB} + C_A L_B R_{LA} f)s^2 + L_B C_A L_A f s^3} \tag{12}$$

Disturbance either from $V_o(s)$, $D(s)$, or $E(s)$ will have the similar behavior because the denominator of (10), (11), and (12) is same. From (10), (11), and (12), relationship between $I_B(s)$, $V_o(s)$, $D(s)$, and $E(s)$ can be derived and is given by (13):

$$I_B(s) = G_{id}(s)D(s) + G_{io}(s)V_o(s) + G_{ie}(s)E(s) \tag{13}$$

Consider the control-to-current transfer function or $G_{id}(s)$ in (10). The denominator of $G_{id}(s)$ is responsible for the occurrence of resonance while the numerator of $G_{id}(s)$ is responsible for the occurrence of anti-resonance. Frequency of resonance and anti-resonance of $G_{id}(s)$ depends on component and linearization point used to derive $G_{id}(s)$. Figure 5 shows Bode plot of $G_{id}(s)$ at various linearization point. The component parameter used to generate Figure 5 is shown in Table 1. Unless stated in the figure itself, the battery voltage, the DC microgrid voltage, and the B-part duty cycle is linearized at 30 V, 30 V, and 2/3 by default. It can be seen from each of Figures 5(a), 5(b), and 5(c) that the resonance increases when the linearization point diverges from aforementioned value. Such resonance can cause instability due to potentially reduced gain margin. Although Figure 5 only shows frequency response of $G_{id}(s)$, it also represents the frequency response of other transfer function such as $G_{ie}(s)$ and $G_{io}(s)$ since the denominator of all those three transfer functions is identical.

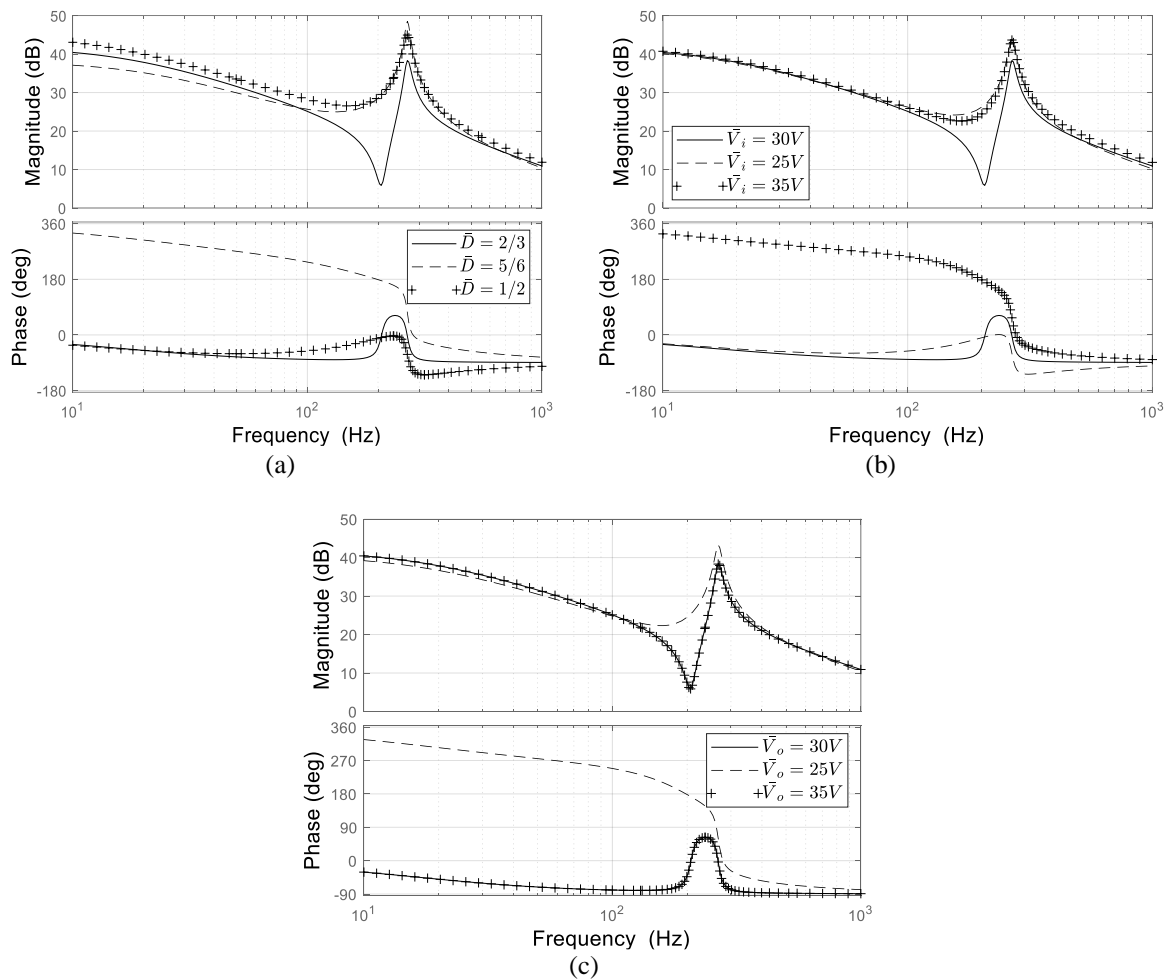


Figure 5. Bode plot of $G_{id}(s)$ at varying (a) \bar{D} , (b) \bar{V}_i , and (c) \bar{V}_o

Table 1. Components of the proposed converter prototype

Parameter	value
A-part Capacitor (C_A)	47 μ F
A-part Inductor (L_A)	4.2 mH
B-part Inductor (L_B)	2.1 mH
Parasitic resistance of L_A (R_{L_A})	0.44 Ω
Parasitic resistance of L_B (R_{L_B})	0.22 Ω

Passive element such as resistor can be used to reduce such resonance [23]. Figure 6 shows the possibility of installing damping resistor on the equivalent model of the proposed converter and its corresponding linearized system block diagram is shown in Figure 7. One of the drawbacks of this method is that more losses is generated due to damping resistor presence. To stabilize the proposed converter without sacrifice the power efficiency, virtual resistor or active damping concept is introduced [24], [25]. The idea of virtual resistor is to mimic physical resistor effect through mathematical manipulation of the converter model so the need to install physical resistor as resonance damper is eliminated. In the case of the proposed converter, only one of damping resistor shown in Figure 6 is needed to be mimicked.

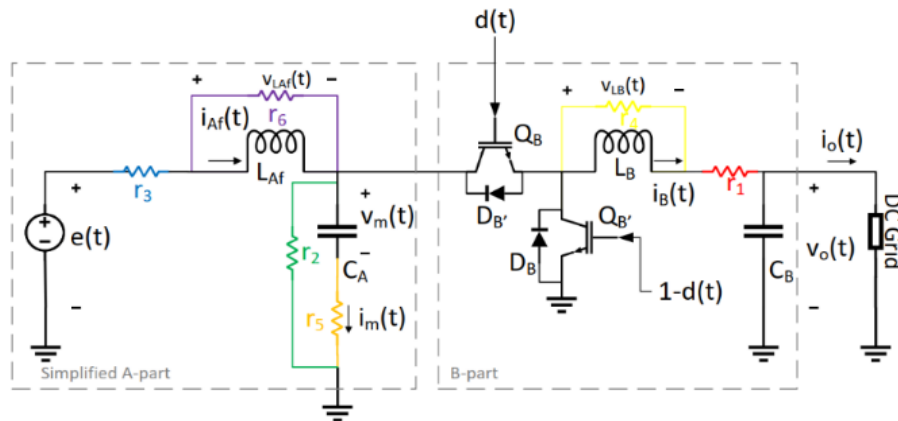


Figure 6. Possibilities of damping resistor locations

Virtual resistor is implemented by rearranging block diagram in Figure 7 into block diagram in Figure 8. The way virtual resistor is implemented is by sensing the required signal and multiply it by an algorithm and then the resulting product is summed with $D^*(s)$. $D^*(s)$ itself will be the same as $D(s)$ if the virtual resistor is not implemented. Algorithm to mimic each damping resistor and their feedback requirements is summarize in Table 2. All algorithm for mimicking the damping resistor is derived under the assumption that parasitic components have negligible effect on the dynamics of the proposed converter system.

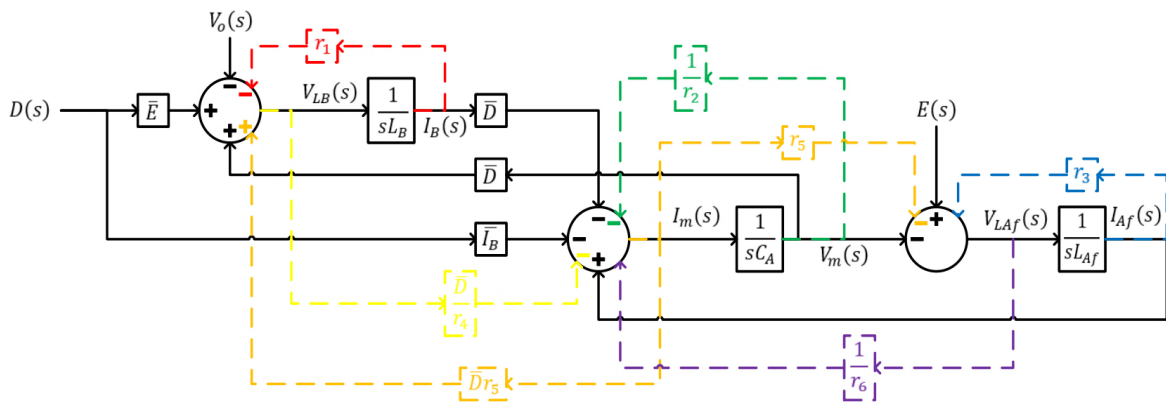


Figure 7. Block diagram of the proposed converter with damping resistor

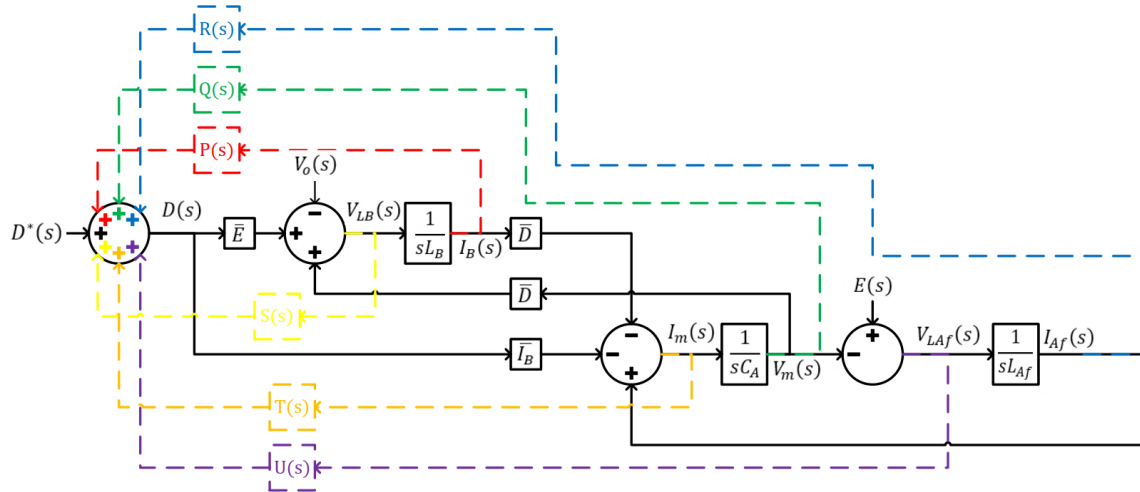


Figure 8. Block diagram of the proposed converter with virtual damping resistor

Table 2. Damping resistor and its virtual resistor algorithm

Damping resistor	Virtual resistor algorithm	Required feedback
r_1	$P(s) = \frac{-r_1(1+s^2L_AfC_A)}{\bar{E}-sL_Af\bar{D}\bar{I}_B+\bar{E}C_AL_Afs^2}$	$I_B(s)$
r_2	$Q(s) = \frac{-\bar{D}L_Afs}{r_2\bar{E}+(\bar{E}L_Af-r_2\bar{D}\bar{I}_BL_Af)s+r_2\bar{E}C_AL_Afs^2}$	$V_m(s)$
r_3	$R(s) = \frac{-\bar{D}r_3}{\bar{E}-\bar{D}\bar{I}_Br_3+(EC_Ar_3-\bar{D}\bar{I}_BL_Af)s+\bar{E}C_AL_Afs^2}$	$I_Af(s)$
r_4	$S(s) = \frac{-L_Af\bar{D}^2s}{r_4(\bar{E}-\bar{D}\bar{I}_BL_Afs+\bar{E}C_AL_Afs^2)}$	$V_B(s)$
r_5	$T(s) = \frac{\bar{D}C_AL_Afr_5s}{\bar{E}+(EC_Ar_5-\bar{D}\bar{I}_BL_Af)s+(EC_AL_Af-\bar{D}\bar{I}_BC_AL_Afr_5)s^2}$	$I_m(s)$
r_6	$U(s) = \frac{\bar{D}L_Afs}{r_6\bar{E}+(\bar{E}L_Af-r_6\bar{D}\bar{I}_BL_Af)s+r_6\bar{E}C_AL_Afs^2}$	$V_Af(s)$

It is necessary to control $i_B(t)$ (and in turn $I_B(s)$) to control the power flow of the proposed converter. This means a sensor is required to sense $i_B(t)$. To fully make use of this sensor, virtual r_1 is selected to damp the peak resonance magnitude because the implementation of virtual r_1 requires the same sensor that have already been used for current control of $i_B(t)$. Another advantage of mimicking r_1 damping resistor instead of other damping resistor is that the numerator of virtual r_1 algorithm (that is $P(s)$, shown in Table 2 doesn't contain \bar{D} which means the damping effect of virtual r_1 won't be affected by whatever value of \bar{D} . Control to current transfer function of the proposed converter which include the effect of virtual r_1 , $G_{id,r1}(s)$, can be obtained by replacing $D(s)$ in (13) with $D^*(s) + P(s)I_B(s)$ and solving for $I_B(s)/D^*(s)$. $G_{id,r1}(s)$ is given by (14).

$$G_{id,r1}(s) = \left. \frac{I_B(s)}{D^*(s)} \right|_{E(s)=0, V_o(s)=0} = \frac{G_{id}(s)}{1-P(s)G_{id}(s)} \tag{14}$$

Battery-to-current transfer function under influence of virtual r_1 , $G_{ie,r1}(s)$, and DC microgrid-to-current transfer function under influence of virtual r_1 , $G_{io,r1}(s)$, can also be obtained by similar fashion and is given by (15) and (16).

$$G_{ie,r1}(s) = \left. \frac{I_B(s)}{E(s)} \right|_{D^*(s)=0, V_o(s)=0} = \frac{G_{ie}(s)}{1-P(s)G_{id}(s)} \tag{15}$$

$$G_{io,r1}(s) = \left. \frac{I_B(s)}{V_o(s)} \right|_{D^*(s)=0, E(s)=0} = \frac{G_{io}(s)}{1-P(s)G_{id}(s)} \tag{16}$$

Similarity between denominator of (14), (15) and (16) implies virtual r_1 also helps in minimizing disturbance effect on the proposed converter. Figure 9 shows root locus of $G_{id,r1}(s)$ due to variation of r_1 . There are two dominant poles and one insignificant pole. To fully stabilize $G_{id,r1}(s)$, these dominant poles must be placed as far as possible from imaginary axis. The farthest dominant pole is obtained $r_1 = 3.39\Omega$ and is marked by red cross on Figure 9. The effect of virtual r_1 on the proposed converter is shown Figure 10. Figure 10(a) to Figure 10(c) shows bodeplot of $G_{id,r1}$, $G_{ie,r1}$, and $G_{io,r1}$. All resonance that occurs at 267 Hz on each of Figure 10(a) to Figure 10(c) due to effect of changing $D^*(s)$, $E(s)$, and $V_o(s)$ is reduced when virtual r_1 implemented. This means virtual r_1 can reduce resonance under various disturbance presence.

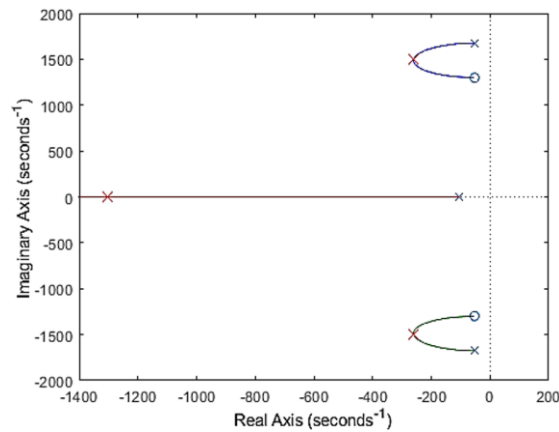


Figure 9. Root locus of $G_{id,r1}(s)$

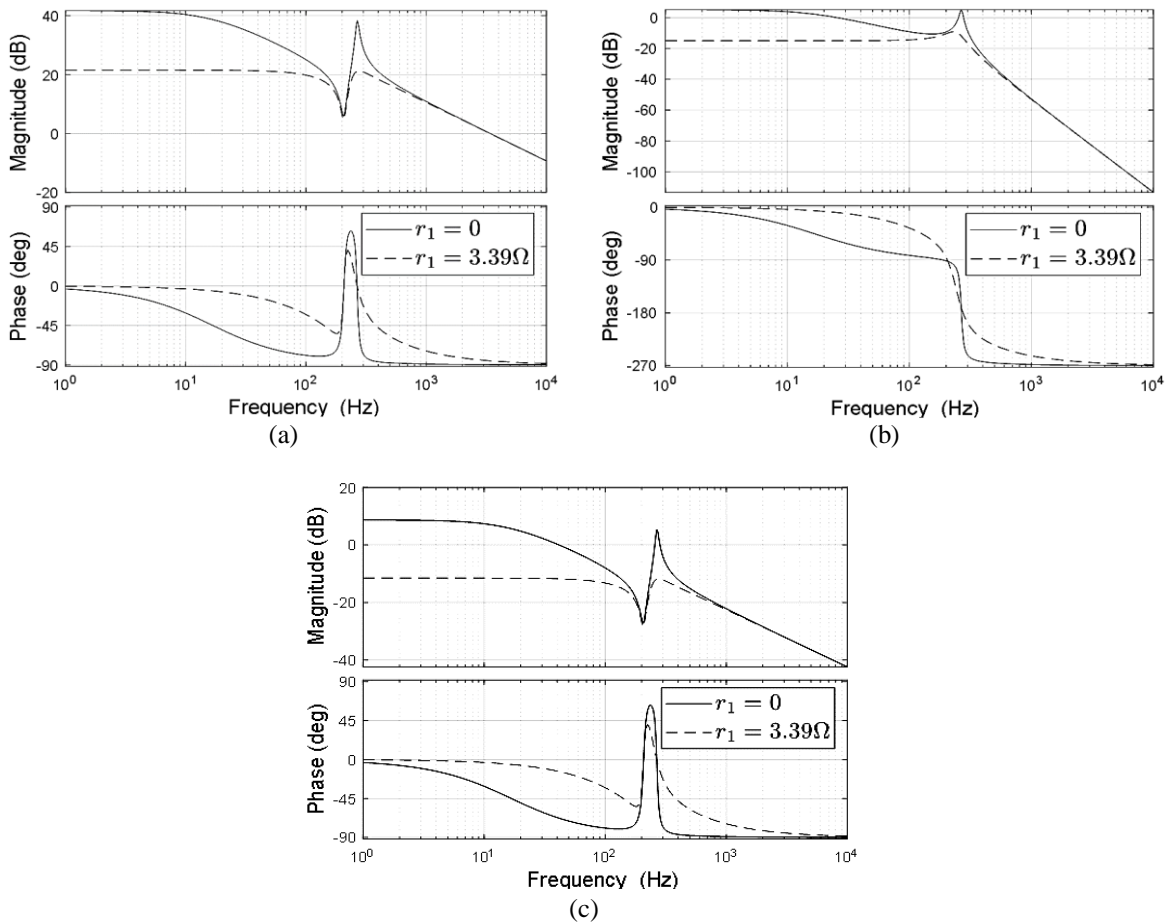


Figure 10. Bode plot of (a) $G_{id,r1}(s)$, (b) $G_{ie,r1}(s)$, and (c) $G_{io,r1}(s)$ at different value of r_1

4. DESIGN OF THE CURRENT CONTROLLER

The current controller must be capable of tracking the current reference $I_B^*(s)$ and reject any disturbances presents. In this paper, a simple proportional-integral (PI) current controller is used. Compensator for implementation of PI current controller is denoted by $G_c(s)$ and is given by (17):

$$G_c(s) = k_p + (k_i/s) \tag{17}$$

where k_p and k_i are proportional and integral constant. $G_c(s)$ itself will be tuned based on $G_{id,r1}(s)$ as its plant with $r_1 = 3.39 \Omega$. Figure 11 shows the current control system of the proposed converter. Here the output of the $G_c(s)$ compensator will be summed with output of virtual resistor algorithm. This means the duty cycle signal entering the B-part's switch is produced by the sum between compensator output and virtual resistor algorithm.

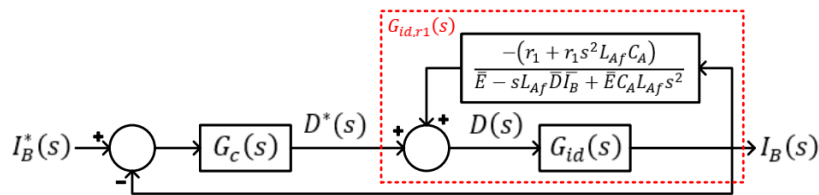


Figure 11. Control system and implementation of virtual resistor

The specification of current controller will be based on gain cross over frequency and phase margin. The gain cross over frequency of the open loop transfer function should be lower than resonance and anti-resonance frequency. Based on Figure 5(a), the resonance and anti-resonance frequency is 267 Hz and 206 Hz therefore the required gain crossover frequency will be 100 Hz. If higher gain crossover frequency is desired, the C_A capacitor should be smaller in value. The phase margin of the open loop transfer function is required to be greater than 60° . Aside from frequency domain requirements, it is also desired to have as low as possible current overshoot in the event of transient. Before tuning of compensator is conducted, operating points and components value of the proposed converter must be determined first. In this paper, the battery voltage, the DC microgrid voltage, and B-part duty cycle is linearized at 30 V, 30 V, and 2/3. The components value used for the purpose of experiment and control design is shown in Table 1. $G_c(s)$ is tuned such that gain crossover frequency of 100 Hz and phase margin of at least 60° is achieved for $G_c(s)G_{id,r1}(s)$ transfer function. With the help of MATLAB, k_p and k_i is found to be 0.05455 and 53.88449. The Bode plot of both compensated and uncompensated $G_c(s)G_{id,r1}(s)$ is shown in Figure 12. Figure 13 shows the Bode plot of closed loop system with and without virtual resistor presence. Figures 13(a), 13(b), and 13(c) shows Bode plot of $I_B^*(s)$ to $I_B(s)$, $E(s)$ to $I_B(s)$, and $V_o(s)$ to $I_B(s)$ transfer function. All plot in Figure 13 shows that virtual resistor presence reduces resonance.

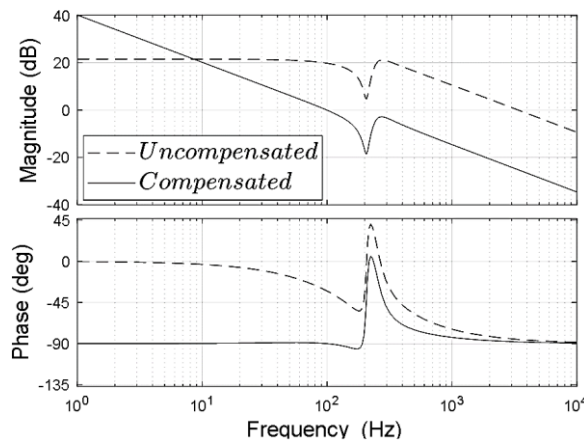


Figure 12. Bode plot of uncompensated and compensated $G_c(s)G_{id,r1}(s)$

At first, the proposed converter is simulated. Compensator used in the simulation is the same as has been derived in previous paragraph. To see reference tracking capabilities of the designed current controller, the proposed converter and its controller is simulated under a changing reference current. The reference current changes its value from 2 A to -2 A representing discharging and charging of the battery connected to this converter. Figure 14 shows simulation result of current control of the proposed converter with a changing reference current. Figure 14(a) shows simulation result if virtual r_1 is installed and has value of $r_1 = 3.39 \Omega$. Figure 14(b) shows the simulation result if virtual r_1 is not installed or $r_1 = 0$. Higher overshoot observed in Figure 14(b) compared to Figure 14(a) shows that the virtual r_1 has effects on stability of the proposed converter. Both Figures 14(a) and 14(b) shows the simulated proposed converter can do bidirectional energy transfer. To see disturbance rejection capabilities of the proposed converter, the proposed converter and its controller is simulated under a changing battery and DC microgrid voltage.

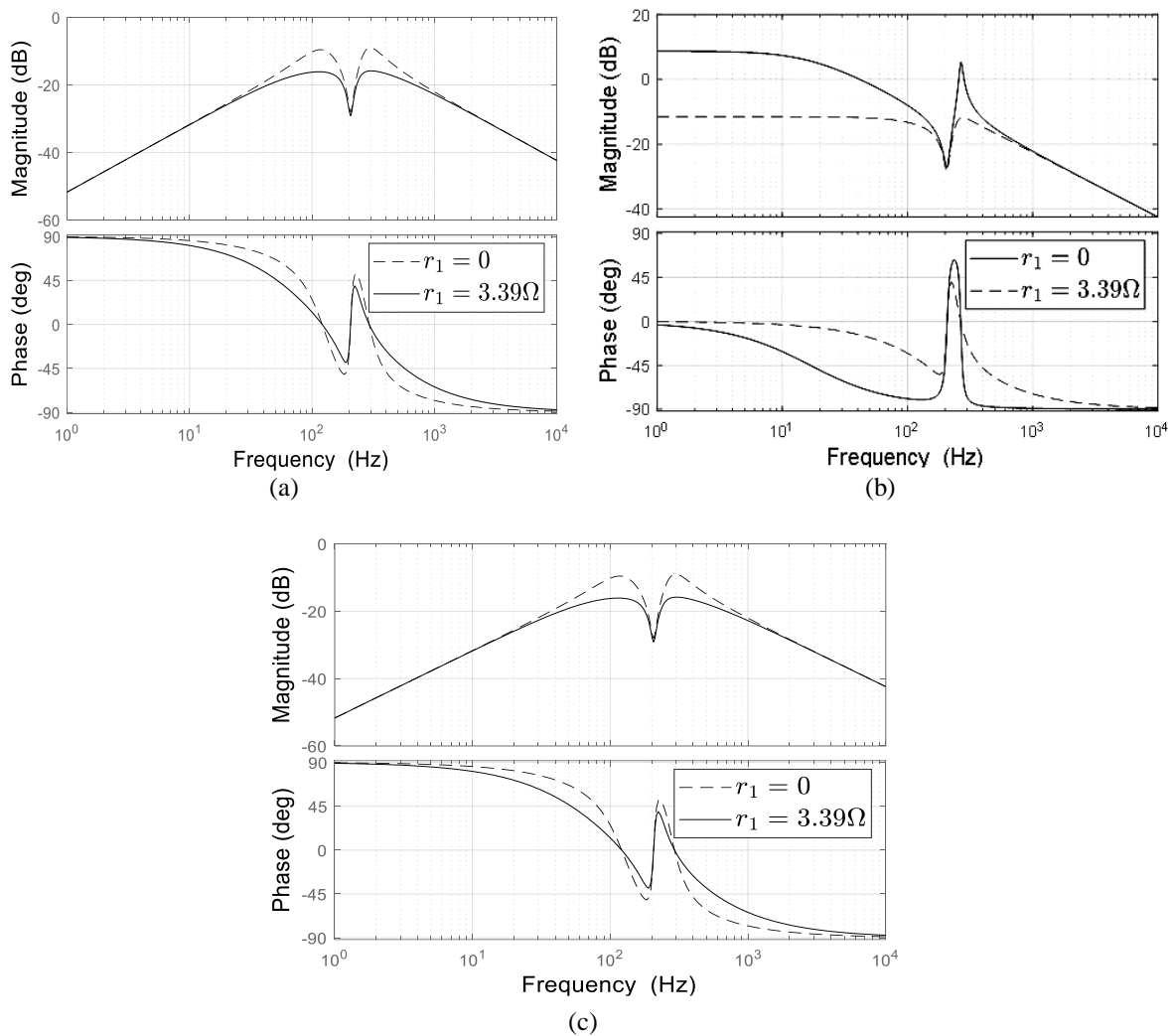


Figure 13. Bode plot of (a) $I_B^*(s)$ to $I_B(s)$, (b) $E(s)$ to $I_B(s)$, and (c) $V_o(s)$ to $I_B(s)$ transfer function at different virtual r_1 value

Figure 15 shows simulation result when the proposed converter is given disturbance at battery and DC microgrid. The upper plot in Figure 15(a) shows $i_B(t)$ and its reference while the lower plot shows fluctuating battery voltage $v_i(t)$. The upper plot in Figure 15(b) shows $i_B(t)$ and its reference while the lower plot shows fluctuating DC microgrid voltage $v_o(t)$. Virtual resistor is implemented in both Figures 15(a) and 15(b). $i_B(t)$ current in both Figures 15(a) and 15(b) follows its reference current despite disturbance presence.

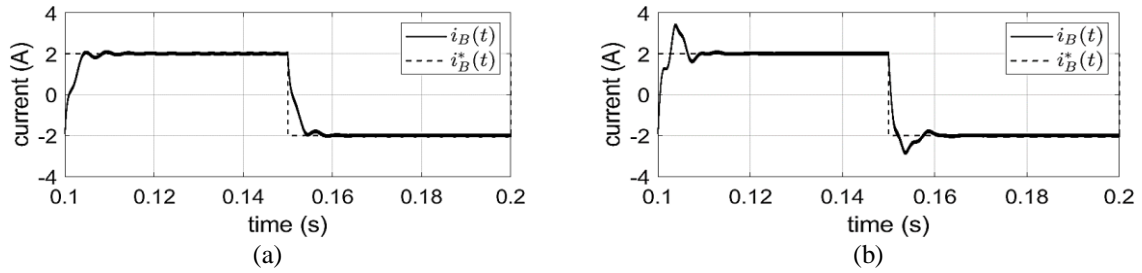


Figure 14. Reference tracking simulation result (a) with virtual resistor and (b) without virtual resistor

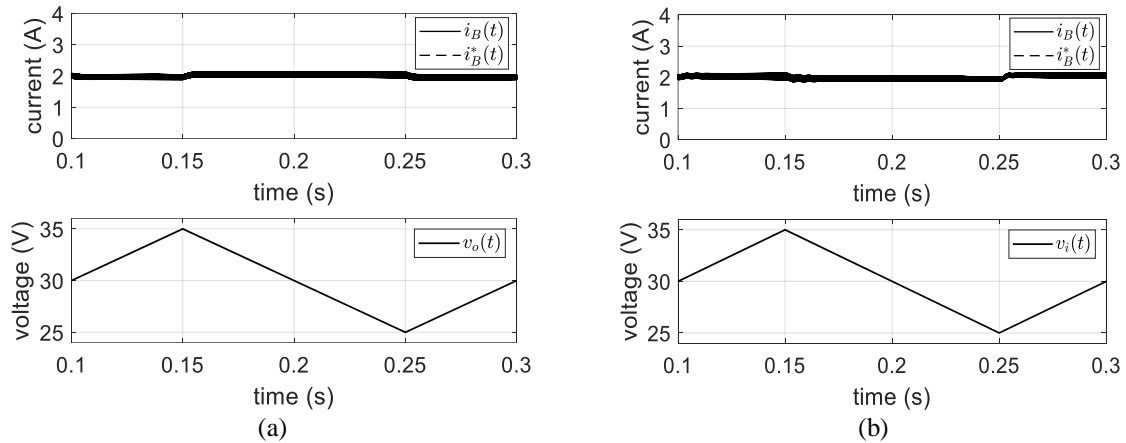


Figure 15. Disturbance rejection simulation result when a disturbance presents at (a) DC microgrid and (b) battery

5. EXPERIMENTAL RESULTS OF THE PROPOSED CONVERTER

Experiment is conducted to see reference tracking and disturbance rejection capabilities of designed control system of the proposed converter. A prototype of the proposed converter used for experimental purpose has been manufactured. The components of the prototype are shown in Table 1. On both side of the prototype, a DC power supply paralleled with a 10Ω load resistor is used to simulate both battery and DC microgrid. Nominal voltage of both battery and DC microgrid is set to be 30 V. The microcontroller used in this experiment for current control is TMS320F28377D. Reference current $i_B^*(t)$ is generated by the microcontroller. Switching frequency of A-part and B-part of the proposed converter is 13.33 kHz and 6.66 kHz. The compensator used in the experiment has the same form as (17) where $k_p = 0.05455$ and $k_i = 53.88449$. The virtual resistor installed to the prototype is virtual r_1 and has value of $r_1 = 3.39 \Omega$.

Figure 16 shows the experimental result for the reference tracking capabilities. The current reference alternate between 2 A and -2 A and is shown by CH2 (cyan). The actual current is shown by CH3 (red). Ampere/div is 1 A and Time/div is 10 ms/div. Figure 16(a) shows experimental result when virtual resistor is installed, and Figure 16(b) shows experimental result when virtual resistor is not installed. Both the battery and DC microgrid is kept at 30 V. +2 A reference current simulates when the battery is discharging and -2 A reference current simulates when the battery is charging. From Figure 16, actual current or $i_B(t)$ tracks its reference whether the the reference is +2 A or -2 A regardless virtual resistor is installed or not but the one with virtual resistor installed has lower overshoot. Besides reference tracking, Figure 16 also shows bidirectional transfer capabilities of the prototype of the proposed converter.

Figure 17 shows the experimental result for disturbance rejection capabilities. The reference current is +2 A and the DC microgrid is given a disturbance. Ampere/div is 1 A/div, Volt/div is 10 V/div, and Time/div is 100 ms/div. The current reference of constant value is shown by CH2 (cyan). The actual current is shown by CH3 (red). The DC microgrid voltage is shown by CH4 (green). While the battery voltage is kept constant at 30 V, the DC microgrid voltage (green line, CH4) is given -10 V disturbance relative to its nominal voltage value. From Figure 17, the actual current is still tracking its reference despite disturbance presence. Although current control for the proposed converter in this paper has been designed using a simple PI controller, it is possible to implement a more sophisticated method such as fuzzy controller [26], [27].

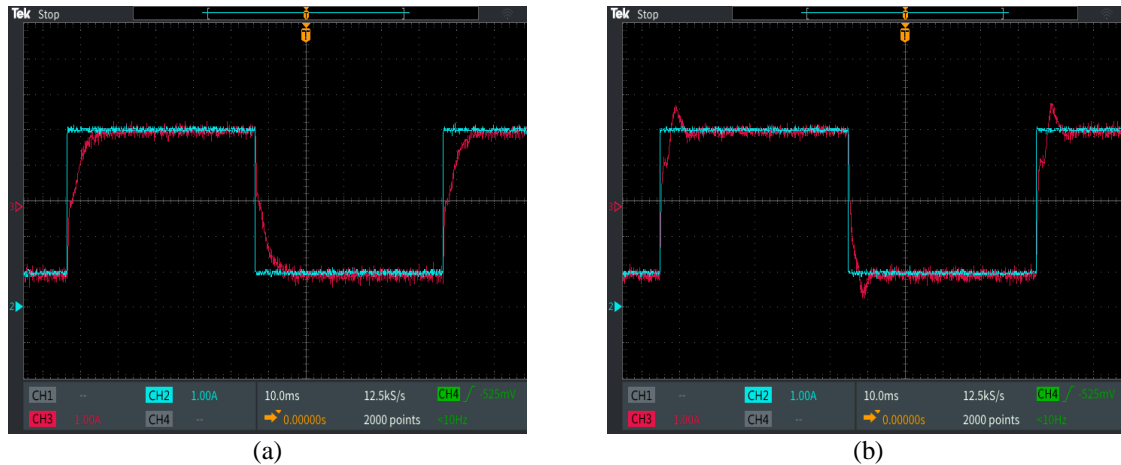


Figure 16. Reference tracking experimental result when (a) virtual resistor presents and (b) virtual resistor does not present

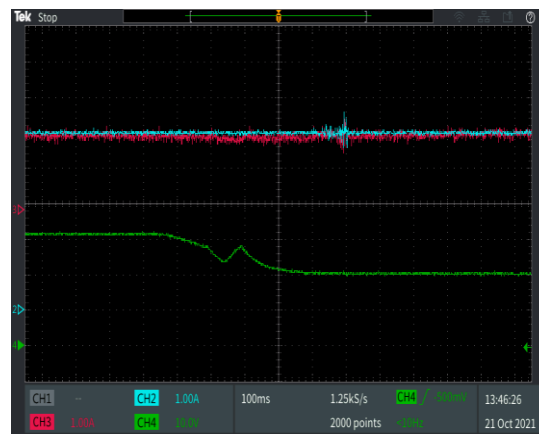


Figure 17. Experimental result when a disturbance presents at DC microgrid

6. CONCLUSION

The proposed converter and its current control strategy for charging and discharging of a battery connected to a DC microgrid with minimized battery ripple current has been presented. How the battery ripple current is minimized has been explained through simulation results. How to use a virtual resistor to damp a transient oscillation has been described. A prototype has been constructed and experiment has been carried out to see the current control capabilities of the proposed converter. Experimental results have shown the effectiveness of the current controller for the proposed converter. Effectiveness of virtual resistor in damping arising resonance in the proposed converter was also shown in the experiment.

ACKNOWLEDGEMENTS

The authors wish to thank the Korea Midland Power Company for the financial support.

REFERENCES




- [1] D. Kumar, F. Zare, and A. Ghosh, "DC microgrid technology: system architectures, AC grid interfaces, grounding schemes, power quality, communication networks, applications, and standardizations aspects," *IEEE Access*, vol. 5, pp. 12230–12256, 2017, doi: 10.1109/ACCESS.2017.2705914.
- [2] T. Dragicevic, X. Lu, J. C. Vasquez, and J. M. Guerrero, "DC Microgrids - Part I: a review of control strategies and stabilization techniques," *IEEE Transactions on Power Electronics*, vol. 31, no. 7, pp. 4876–4891, 2016, doi: 10.1109/TPEL.2015.2478859.
- [3] T. Dragičević, X. Lu, J. C. Vasquez, and J. M. Guerrero, "DC microgrids - Part II: a review of power architectures, applications, and standardization issues," *IEEE Transactions on Power Electronics*, vol. 31, no. 5, pp. 3528–3549, 2016, doi: 10.1109/TPEL.2015.2464277.
- [4] A. Sharma and S. Sharma, "Review of power electronics in vehicle-to-grid systems," *Journal of Energy Storage*, vol. 21,

A current control method for bidirectional multiphase DC-DC boost-buck converter (Gifari Iswandi Hasyim)




- no. November 2018, pp. 337–361, 2019, doi: 10.1016/j.est.2018.11.022.
- [5] E. Martinez-Laserna *et al.*, “Battery second life: hype, hope or reality? a critical review of the state of the art,” *Renewable and Sustainable Energy Reviews*, vol. 93, no. February 2017, pp. 701–718, 2018, doi: 10.1016/j.rser.2018.04.035.
 - [6] M. Broussely *et al.*, “Main aging mechanisms in Li ion batteries,” in *Journal of Power Sources*, 2005, vol. 146, no. 1–2, pp. 90–96, doi: 10.1016/j.jpowsour.2005.03.172.
 - [7] W. Waag, S. Käbitz, and D. U. Sauer, “Experimental investigation of the lithium-ion battery impedance characteristic at various conditions and aging states and its influence on the application,” *Applied Energy*, vol. 102, pp. 885–897, 2013, doi: 10.1016/j.apenergy.2012.09.030.
 - [8] K. Uddin, A. D. Moore, A. Barai, and J. Marco, “The effects of high frequency current ripple on electric vehicle battery performance,” *Applied Energy*, vol. 178, pp. 142–154, 2016, doi: 10.1016/j.apenergy.2016.06.033.
 - [9] P. A. Dahono, S. Riyadi, A. Mudawari, and Y. Haroen, “Output ripple analysis of multiphase dc-dc converters,” in *Proc. of the International Conference on Power Electronics and Drive Systems*, 1999, vol. 2, pp. 626–631, doi: 10.1109/peds.1999.792732.
 - [10] H. B. Shin, J. G. Park, S. D. Chang, and H. C. Choi, “Generalized analysis of multi-phase interleaved boost converter,” *International Journal of Electronics*, vol. 92, no. 1, pp. 1–20, 2005, doi: 10.1080/00207210412331332943.
 - [11] M. A. Khan, A. Ahmed, I. Husain, Y. Sozer, and M. Badawy, “Performance analysis of bidirectional DC-DC converters for electric vehicles,” *IEEE Trans. on Industry App.*, vol. 51, no. 4, pp. 3442–3452, 2015, doi: 10.1109/TIA.2015.2388862.
 - [12] S. Saponara and L. Mihet-Popa, “Energy storage systems and power conversion electronics for e-transportation and smart grid,” *Energies*, vol. 12, no. 4, pp. 1–9, 2019, doi: 10.3390/en12040663.
 - [13] S. A. Gorji, H. G. Sahebi, M. Ektesabi, and A. B. Rad, “Topologies and control schemes of bidirectional DC–DC power converters: an overview,” *IEEE Access*, vol. 7, pp. 117997–118019, 2019, doi: 10.1109/ACCESS.2019.2937239.
 - [14] M. A. Khan, I. Husain, and Y. Sozer, “A bidirectional DC–DC converter with overlapping input and output voltage ranges and vehicle to grid energy transfer capability,” *IEEE Journal of Emerging and Selected Topics in Power Electronics*, vol. 2, no. 3, pp. 507–516, 2014, doi: 10.1109/jestpe.2014.2305157.
 - [15] I. Aharon, A. Kuperman, and D. Shmilovitz, “Analysis of dual-carrier modulator for bidirectional noninverting buck-boost converter,” *IEEE Transactions on Power Electronics*, vol. 30, no. 2, pp. 840–848, 2015, doi: 10.1109/TPEL.2014.2315993.
 - [16] D. W. Spier, G. G. Oggier, and S. A. O. da Silva, “Dynamic modeling and analysis of the bidirectional DC-DC boost-buck converter for renewable energy applications,” *Sustainable Energy Technologies and Assessments*, vol. 34, no. April, pp. 133–145, 2019, doi: 10.1016/j.seta.2019.05.002.
 - [17] S. Waffler and J. W. Kolar, “A novel low-loss modulation strategy for high-power bidirectional buck + boost converters,” *IEEE Transactions on Power Electronics*, vol. 24, no. 6, pp. 1589–1599, 2009, doi: 10.1109/TPEL.2009.2015881.
 - [18] M. Gaboriault and A. Notman, “A high efficiency, non-inverting, buck-boost DC-DC converter,” in *Conf. Proc. IEEE Applied Power Electronics Conference and Exposition - APEC*, 2004, vol. 3, no. C, pp. 1411–1415, doi: 10.1109/apec.2004.1296049.
 - [19] S. Waffler, J. Biela, and J. W. Kolar, “Output ripple reduction of an automotive multi-phase Bi-directional DC-DC converter,” *2009 IEEE Energy Conversion Congress and Exposition*, pp. 2184–2190, 2009, doi: 10.1109/ECCE.2009.5316346.
 - [20] M. Y. Metwly, M. S. Abdel-Majeed, A. S. Abdel-Khalik, R. A. Hamdy, M. S. Hamad, and S. Ahmed, “A review of integrated on-board EV battery chargers: advanced topologies, recent developments and optimal selection of FSCW slot/pole combination,” *IEEE Access*, vol. 8, pp. 85216–85242, 2020, doi: 10.1109/ACCESS.2020.2992741.
 - [21] T. Na, X. Yuan, J. Tang, and Q. Zhang, “A review of on-board integrated charger for electric vehicles and a new solution,” *2019 IEEE 10th Int. Symp. on Power Electronics for Distributed Generation Systems (PEDG)*, vol. 4, no. 4, pp. 693–699, 2019, doi: 10.1109/PEDG.2019.8807565.
 - [22] R. D. Middlebrook and S. Cuk, “A general unified approach to modelling switching-converter power stages,” in *1976 IEEE Power Electronics Specialists Conference*, Jun. 1976, vol. 21, no. 1, pp. 18–34, doi: 10.1109/PESC.1976.7072895.
 - [23] M. Cespedes, L. Xing, and J. Sun, “Constant-power load system stabilization by passive damping,” *IEEE Transactions on Power Electronics*, vol. 26, no. 7, pp. 1832–1836, 2011, doi: 10.1109/TPEL.2011.2151880.
 - [24] P. A. Dahono, “A control method for DC-DC converter that has an LCL output filter based on new virtual capacitor and resistor concepts,” in *IEEE 35th Annual Power Electronics Specialists Conference*, 2004, vol. 1, pp. 36–42, doi: 10.1109/pesc.2004.1355709.
 - [25] A. Rizqiawan, R. Nasution, P. Argo Dahono, and T. D. Rachmildha, “Damping improvement by using virtual resistance controller for DC-DC boost converter dahono-1,” *International Conference on High Voltage Engineering and Power Systems, ICHVEPS 2017 - Proceeding*, vol. 2017-Janua, pp. 400–403, 2017, doi: 10.1109/ICHVEPS.2017.8225878.
 - [26] W. Dwiono, “Fuzzy PI controllers performance on boost converter,” *International Journal of Electrical and Computer Engineering (IJECE)*, vol. 3, no. 2, pp. 215–220, 2013, doi: 10.11591/ijece.v3i2.2262.
 - [27] C. T. Manikandan and G. T. Sundarajan, “Fuzzy logic controller for closed loop cascaded flyback converter fed pm-dc-motor system,” *International Journal of Power Electronics and Drive Systems (IJPEDS)*, vol. 11, no. 4, pp. 1857–1865, 2020, doi: 10.11591/ijpeds.v11i4.pp1857-1865.

BIOGRAPHIES OF AUTHORS






Gifari Iswandi Hasyim    He received his bachelor’s degree in Electrical Power Engineering from Institut Teknologi Bandung, in 2016. His field of research is Power Electronic. At present, he is a graduate student at Institut Teknologi Bandung. He can be contacted at email: gifarihasyim@gmail.com.






Sulistyo Wijanarko    He received his bachelor's degree in Electrical Engineering from Universitas Gadjah Mada, in 2013. His field of research is Power Electronic and Drives. At present, he is a graduate student at Institut Teknologi Bandung and a researcher at Indonesian Institute of Sciences. He can be contacted at email: sulis.wijanarko@gmail.com.






Jihad Furqani    was born in Malang, East Java, Indonesia in 1990. He received B.S. degree in Electrical Power Engineering from Bandung Institute of Technology in 2012. He received M.S. degree in Electrical Engineering from Bandung Institute of Technology in 2013. He received Dr. Eng. degree in Electrical and Electronic Engineering from Tokyo Institute of Technology in 2019. He has been studying multilevel and multiphase motor drive, noise reduction in switched reluctance motor, power electronic converter for renewable energy application, and electric motor for vehicle application. He was Visiting Researcher of University of Akron in 2017 and Visiting Lecture of Tokyo Institute of Technology in 2021. Currently, he is lecturer in Electrical Power Engineering, School of Electrical Engineering and Informatics, National Center for Sustainable Transportation Technology, and Center for Instrument Technology and Automation, Bandung Institute of Technology. He received IEEE Star Reviewer in 2019. He can be contacted at email: j.furqani@konversi.ee.itb.ac.id.



Arwindra Rizqiawan    He received his bachelor and master's degree from Insitut Teknologi Bandung, Indonesia, in 2006 and 2008, respectively, and doctoral degree from Shibaura Institute of Technology, Japan, in 2012, all in the field of electrical engineering. His current main interests are power engineering, power electronics, and renewable energy. He is currently serving as assistant professor in School of Electrical Engineering and Informatics, Institut Teknologi Bandung, Indonesia. He is a certified professional engineer (IPM) in Indonesia by the Institution of Engineers Indonesia (PII), and ASEAN Engineer by ASEAN Engineering Register. He can be contacted at email: windra@staff.stei.itb.ac.id.



Pekik Argo Dahono    He got the Insinyur (Ir) degree, from the Institut Teknologi Bandung, Indonesia, in 1985, the Master and Doctor Engineering degrees from Tokyo Institute of Technology, Japan, in 1992 and 1995, respectively, all in electrical engineering. He is registered as a Professional Engineer in Indonesia and ASEAN. He is a senior member of IEEE. He is a cofounder of Indonesia Smart Grid Initiatives and Indonesia Power Quality Initiatives. At present, he is a professor in the School of Electrical Engineering and Informatics, Institut Teknologi Bandung. He has interest in power electronics, power systems, and power quality. He can be contacted at email: pekik@konversi.ee.itb.ac.id.